Electron beam profile: Experiment, simulation configuration, and application for ETS-10 zeolite irradiated simulation

Cao Van Chung,[1,*] La Ly Nguyen,[2] Lo Thai Son,[2] Anh-Tuan Vo,[1] Van-Hien Pham,[3,4] Phan Trong Phuc,[2,†] and Van-Phuc Dinh[5,‡]

[1]*Research and Development Center for Radiation Technology, Ho Chi Minh City 700000, Vietnam*
[2]*Center for Nuclear Technologies, Vietnam Atomic Energy Institute, Ho Chi Minh City 700000, Vietnam*
[3]*Institute of Advanced Technology, VAST, TL29, Thanh Loc Ward, District 12, Ho Chi Minh City 700000, Vietnam*
[4]*Graduate University of Science and Technology, VAST, TL29, Thanh Loc Ward, District 12, Ho Chi Minh City 700000, Vietnam*
[5]*Institute of Interdisciplinary Sciences, Nguyen Tat Thanh University, Ho Chi Minh City 700000, Vietnam*

(Received 28 January 2025; accepted 21 May 2025; published 12 June 2025)

We present a simulation configuration for the electron beam profile consistent with experiments on the linear accelerator UERL-10-15S2, focusing on determining electron energy and beam size. Two essential aspects of the electron beam described in the simulation configuration are the initial energy distribution and the initial beam size with the flux distribution. Notably, we introduce a new mathematical function by modifying the approximated Landau distribution. This new function offers a better fit than our previous mathematical function and, more importantly, accurately reflects the physical nature of the energy spectrum of electrons passing through a thin layer of matter. Using this configuration, we have simulated the irradiation of zeolite ETS-10 by the electron beam. This irradiated simulation was set up with various electron energy distributions, yielding results on the dose rate distribution (2D dose map) and the mean absolute percentage deviation of the absorbed dose rate within the irradiated titanosilicate. With the improvements in this paper, we have provided a solution to enhance the linear accelerator's application in scientific research besides conventional industrial irradiation applications.

DOI: 10.1103/dpc5-cgh4

I. INTRODUCTION

Irradiation, which involves exposing materials to ionizing radiation, was first used over a century ago [1]. In the 1950s, the discovery that ionizing radiation would enhance the value of polyethylene opened the way for full-scale commercial use of electron beam accelerators [2]. Today, there are more than 800 industrial irradiation facilities worldwide [3]. These facilities use gamma rays emitted from ^{60}Co source or high-energy electrons from linear accelerators. One of the above-mentioned linear accelerator (linac) systems is the UERL-10-15S2 model equipped at our facility for industrial applications: irradiation of foods, fruits, and medical devices. Besides industrial purposes, the accelerator system is also used in scientific research. Some studies directly serve industrial irradiation purposes, such as researching the dose uniformity ratio (DUR) in the irradiation of food products or star apple fruit [4,5]. Another important application branch of these linacs is the research on material modification.

Electron beam (e-beam) irradiation is a physical approach used to modify the structure of various materials, such as polymer [6], zeolite A, X, Y, and ZSM-5 [7], natural zeolite [8], Ca-A zeolite [9], Na-A zeolite [10], and activated carbon [11]. Research results show that, when irradiating with a high-energy e-beam, chemical transformation occurs due to the influence of electrons on atoms, causing them to be excited, ionized, or displaced in the structure, resulting in increased defects. This increase in defects enhances the catalytic and adsorption properties of the material. Researchers have also applied this method to many materials in other fields, such as carbon nanotubes, graphene, and diamond [12–15].

Zeolites are materials formed by $Si(X)O_4$ units (X atom is Al or Ti) coordinated tetrahedrally through O bridges [16]. They are microporous crystalline aluminosilicates (or titanosilicates) with a framework structure consisting of

*Contact author: chungvinagamma@gmail.com
†Contact author: phantrongphuc84@gmail.com
‡Contact author: dvphuc@ntt.edu.vn

$Si(Al)O_4$ [or $Si(Ti)O_4$] tetrahedral units [17]. They have a framework structure of channels and pores with high uniformity and are suitable for use as molecular sieves, supporting nanoparticle catalysts. This material is becoming more advanced regarding framework structure, morphology, and chemical composition. Due to their unique properties, including shape selectivity, adsorption, and ion exchange, zeolites have played a significant role in advancing numerous industrial processes in catalysis, adsorption, and gas separation [18,19]. Synthetic methods producing large quantities of pure zeolites with well-defined crystal structures still rely on the use of organic amines and quaternary ammonium ions as structure-directing agents (SDAs) (or templates in some texts) [20,21]. The SDA molecules filling the voids in the completed crystal structures must be removed before the ion exchange and activation step. To burn off these trapped SDAs and subsequently activate the zeolites for use as catalysts or adsorbents, high temperature (773–923 K) for long periods is often used (called conventional calcination). However, this approach has led to many adverse effects on the material, such as structural deterioration, disordered arrangement of the porous structure [22], and loss of framework structure [23]. Electron irradiation can be considered a potential solution to break down SDA organic molecules in zeolite materials at sufficiently low temperatures [24]. The advantages of this method are that it has no limit on the sensitivity of the e-beam, has a low electron irradiation dose, and has high-energy efficiency. Besides, electron irradiation is a promising method for modifying the structure and activity of catalysts by creating new types of active sites on the catalyst surface, which results in more activated and selective catalysts [19]. Therefore, studying the impact of e-beam irradiation on materials, particularly zeolite ETS-10, is crucial for uncovering how these irradiation-induced structural changes enhance the material's functionality across diverse applications. By exploring the modifications in ETS-10 titanosilicate through irradiation, we can improve its properties, significantly broadening its potential uses in industry and environmental management.

Understanding the characteristics of electron beams is crucial, especially when high-dose irradiated samples are exposed to them for extended periods. Typically, after the e-beam passes through the titanium window of the scan horn, it disperses at an opening angle. The dose distribution, or irradiation field, observed at a certain distance from the scan horn follows a Gaussian distribution. Depending on each linac's characteristics and the titanium window's thickness, the e-beam can have different sizes determined by the FWHM of the above Gaussian spectrum. For industrial irradiation, operational qualification requires determining the electron beam's stability and the product's dose distribution (depth-dose profile). Therefore, determining the energy of the electron beam after acceleration and the beam size is important in determining the depth-dose profile, maximum speed of the conveyor system, and scanning frequency [25,26]. Moreover, the growing use of accelerator devices in research has led to the need to construct simulation configurations that accurately represent beam profiles, fulfilling the demand for precision in applying these devices to scientific inquiry. However, in previous studies [5,27,28], the conventional beam profile configuration was simplified (considering the electron source as monoenergetic and homogeneous flux distribution).

This study aims to develop an enhanced simulation configuration for the beam profile, validated through experiments on e-beam quality using B3 dosimeters. This improved configuration is based on two important aspects of the e-beam: initial energy distribution and initial beam size, including the flux distribution. The paper also details the procedures for assessing the beam quality of the linac system, which include setting up measurements to determine the electron beam energy distribution and the beam size. This is particularly relevant for small-sized samples that require high irradiated doses and remain stationary during the irradiation process. By experimentally determining the electron energies with different electron energy distributions ranging from 6 to 10 MeV, we also checked the measurement method's response to different electron energy distributions. Another notable improvement was made by proposing a new mathematical function to replace the previous one [28]. The new function was employed to better fit the energy remains of electrons passing through a thin layer of matter. It outperforms the old ansatz function and accurately describes the physics behind the formation of the energy distribution of degraded electrons. The confirmation between Monte Carlo simulation and experiment helps to enhance and expand the application of industrial irradiation linac systems in scientific research, specifically the irradiation of zeolite materials. In the last simulation section, we applied this specified beam profile configuration to simulate and determine the dose map and mean absolute percentage deviation of the absorbed dose rate in the irradiation of zeolite ETS-10. This analysis provides solutions for optimizing the experimental irradiation of this type of material.

II. METHODOLOGY

This research was conducted using the linac model UERL-10-15S2, provided by Corad Services Ltd., Russia, and operated at the Research and Development Center for Radiation Technology in Vietnam. This linac model accelerates electrons with high frequencies through the resonator of its accelerating structure. The nominal energy of the electrons after acceleration is 10 MeV, the beam has pulse frequency ranging from 1 to 300 Hz, a beam pulse with a duration of 16 μs, and beam average current of 720 μA for 7.5 kW beam power. The oscilloscope traces

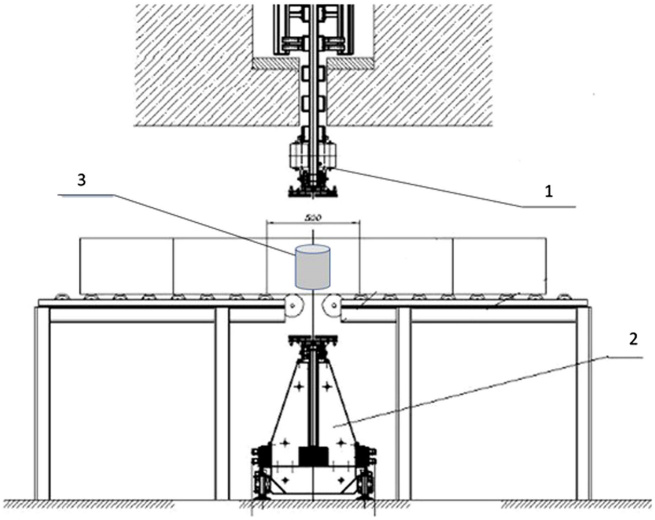

FIG. 1. Two scanners of the UERL-10-15S2 linear accelerator: (1) Scanner 1_upper scan horn, (2) Scanner 2_lower scan horn, and (3) irradiated sample.

of beam signals can be found in the Appendix (Fig. 13). The device features two symmetrical scanners (see Fig. 1) and provides an uncertainty of dose uniformity of 5%, along with energy stability (uncertainty of energy) of 2.5% [5]. A series of experimental measurements were performed to investigate the beam quality. In these experiments, the linac system was set up in single-sided mode, projecting e-beam downward from Scanner 1_upper scan horn. Simultaneously, a simulation configuration of the initial beam at the scanner output was also set up.

A. Experiments determining beam profile

1. Experiments determining electron energy distribution

The experiments were conducted using Riso Wedge [29] and B3 dosimeters [30] (Fig. 2). In addition to the experiments to determine the electron energy directly from the scanner and 30 cm away from the scanner, we also investigated the electron energy attenuation through aluminum alloy 1050 plates with different thicknesses of 0.3, 0.5, and 0.8 cm. We investigated the attenuation distribution of electron energy through aluminum plates due to our design of the ETS-10 sample holder with an aluminum alloy in the simulation Sec. II C. Furthermore, we aimed to assess the measurement method's response to varying electron energy distributions.

After irradiation, the B3 dosimeters were heat treated for 15 min to stabilize the dosimeter absorbance. Then, the dosimeters were measured at a fixed wavelength of 552 nm $\pm$ 2 nm using a spectrophotometer: GENESYS 30 (Fig. 3) and dose values were recorded using DoseControl software according to the procedure [31]. From the above dose results, we established a depth-dose curve, and then, we fit a trendline from which the R_p (practical range) and R_{50} (half-value depth) were estimated. Next, the E_p—electron's most probable energy and E_a—average energy values were calculated from the above R_p and R_{50} values using second-order equations [Eqs. (1) and (2)] [26]. An illustration of this data processing process is shown visually in Fig. 4.

$$E_p(\mathrm{MeV}) = 0.256 + 4.91\,R_p - 0.0248R_p^2, \qquad (1)$$

$$E_a(\mathrm{MeV}) = 0.297 + 6.61R_{50} - 0.325R_{50.}^2 \qquad (2)$$

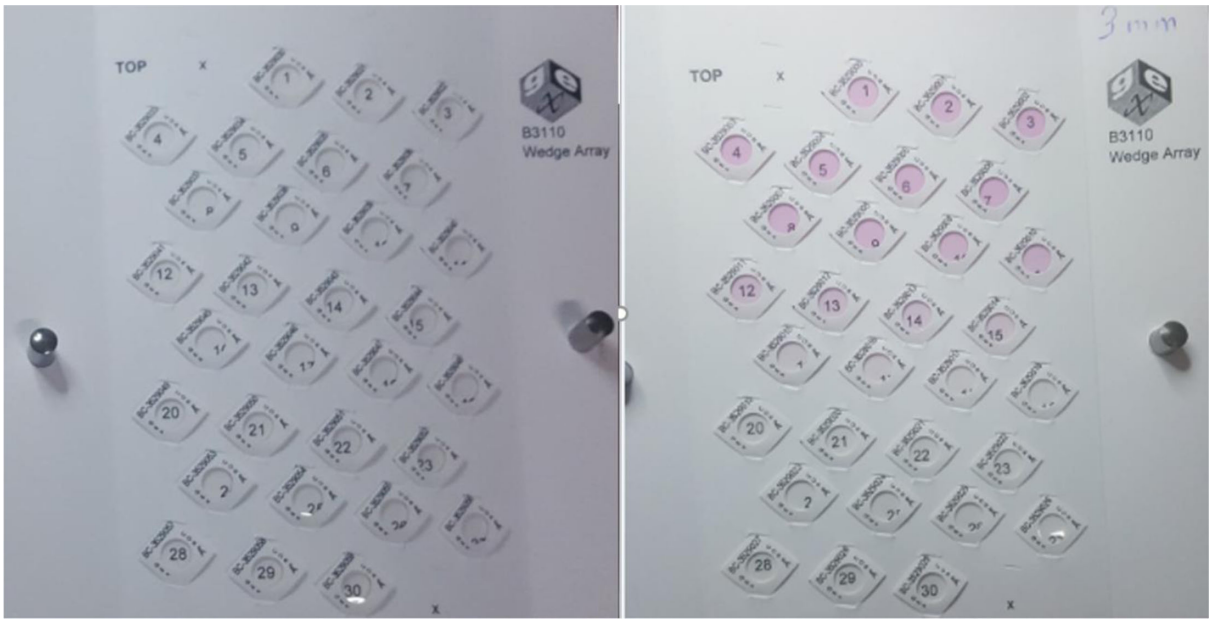

FIG. 2. B3 dosimeters on the B3110 Wedge Array before and after the irradiation.

FIG. 3. Spectrophotometer: GENESYS 30 at our facility.

2. *Experiments determining beam size*

To investigate the beam size, we arranged a series of dosimeters [32] as shown in Fig. 5. Due to the technical characteristics of ensuring the safety of the equipment, it is not possible to emit the electron beam at a position that stops straight down to fully determine the beam spot (affecting the integrity of the titanium window, possibly overheating and causing the window to perforate). Therefore, we decided to investigate the beam size in a single scanner mode and without running the conveyor: stationary, single-sided mode.

Since each B3 dosimeter has a standard size of 1 cm, the consecutive arrangement of B3 dosimeters creates a distance between the centers of the dosimeters of 1 cm; it is impossible to survey the dose point with a smaller distance. To overcome this, the dosimeters were arranged in a staggered manner, reducing the distance between the measuring points to 0.5 cm (Fig. 5). B3 strips with appropriate dosimeter spacing were fixed at distances from the scan horn of 20, 30, 45, and 60 cm and perpendicular to the scanning direction of the electron beam for a period of 8 to 10 s to record the dose value. Then, the dose distribution was determined, and based on this distribution, we reconstructed the beam size.

B. Simulation

Monte Carlo simulations of electron transport were performed using the licensed MCNP 6.3 software [33]. The method of constructing the beam profile is based on the theoretical basis of the radio-frequency (rf) accelerator system, using the resonators of the accelerating structure, and on the actual characteristics of the UERL-10-15S2 system at our facility. We selected the parameters and constructed the appropriate electron beam profile configuration.

The electron source configuration, or initial beam profile, constructed in our simulations consists of two important aspects: the initial electron energy distribution and the initial beam size with the flux distribution. In the rf linac model, the electron energy after acceleration will not be monoenergetic. Due to the accelerating structure, electrons passing through the first resonant cavities will be gathered into bunches of a specific size. Each bunch of electrons will continue to be accelerated in the subsequent resonant cavities, resulting in an electron energy distribution for each bunch after acceleration that takes the shape of a sharp peak with both long and short tails [34]. The initial electron energy distribution for this simulation was constructed in a similar form using a histogram distribution [Fig. 6(a)]. The electron's bunches will then pass through a series of magnetic lenses, so the size of the initial beam spot is not focused and will be a truncated Gaussian distribution [26]. This simulation also constructed the size and flux

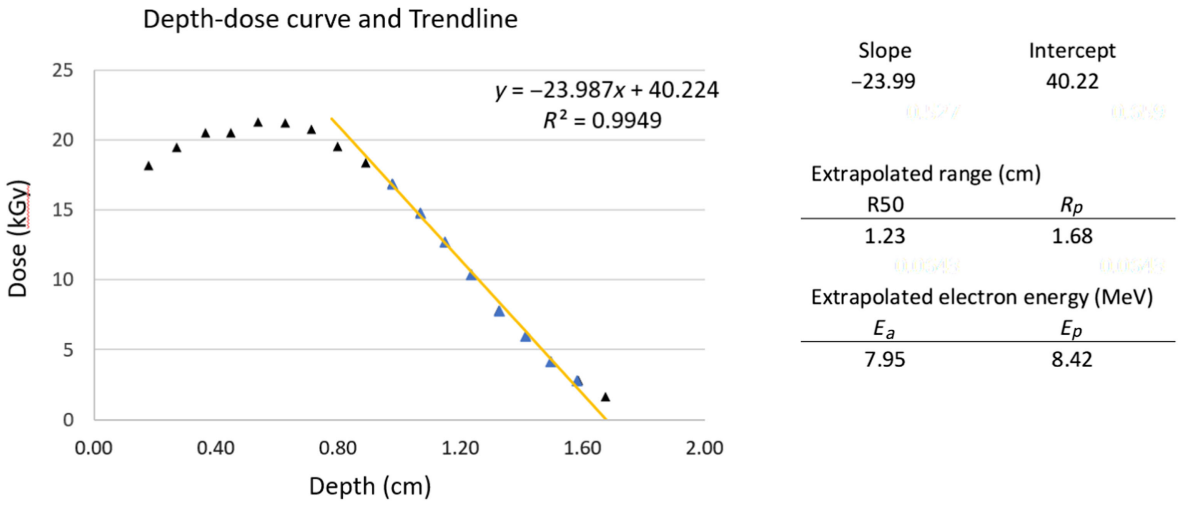

FIG. 4. Depth-dose curve and extrapolated electron energies of the degraded e-beam passing 0.3 cm Al alloy plate.

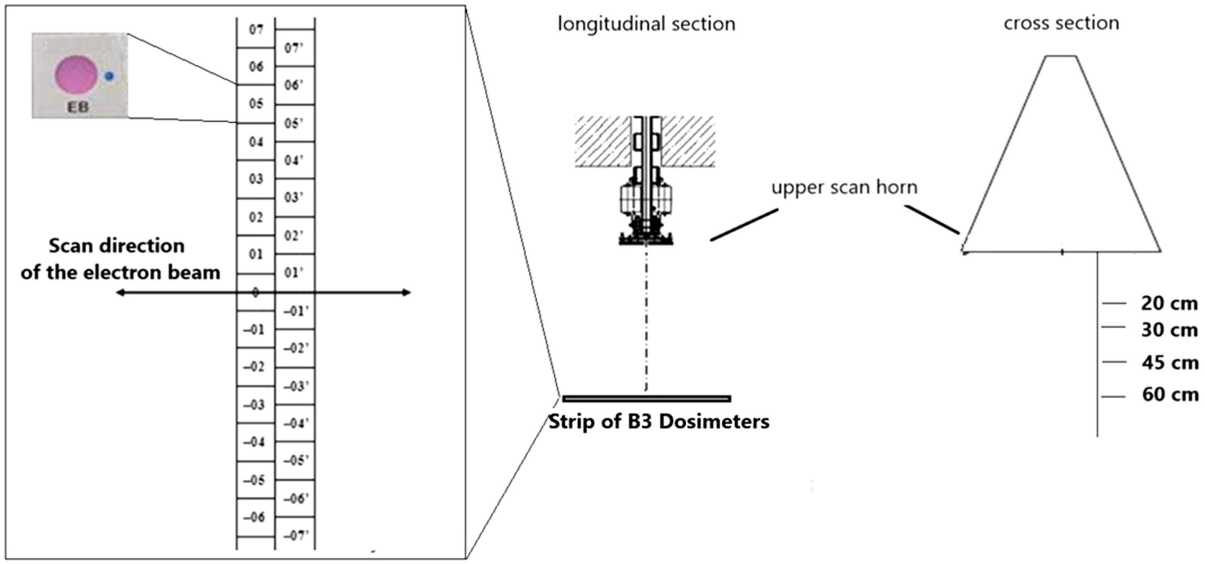

FIG. 5. Experimental design to determine beam size.

distribution of this initial beam spot according to the histogram distribution [Fig. 6(b)], which approximates the truncated Gaussian distribution mentioned above. Due to the effect of a layer of titanium window, this e-beam diverges slightly when leaving the scanner.

With the initial beam setup as above, we simulated the experimental measurements using stationary, single-sided mode to determine the beam size and electron energy. The horizontal scanning effect of the beam can be neglected when the size of the irradiated object is small compared to the scanner's scanning width. Throughout this simulation research, we use the pulse height tally (tally F8) to investigate the electron beam energy distribution and beam size at distances to the scanner, similar to the experiments. Specifically, in the e-beam energy distribution survey simulation, the tally F8 was placed 30 cm from the scan horn. It recorded the energy distribution of electrons directly from the scanner and of electrons after passing through 0.3, 0.5, and 0.8 cm Al alloy plates.

For the beam size simulation, we utilized F8 tallies arranged in concentric rings, with each ring's radius corresponding to the spacing of the B3 dosimeters (B3 strip) in the

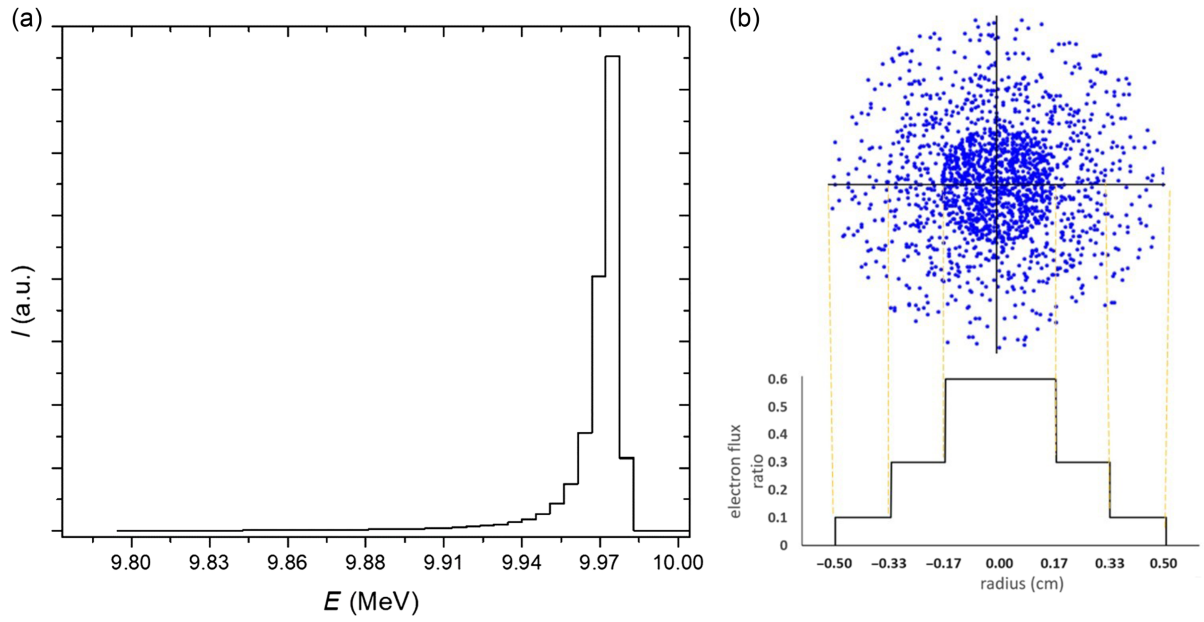

FIG. 6. (a) Histogram distribution of electron source's energy (before passing titanium window): maximum kinetic energy: 9.98 MeV, average kinetic energy: 9.96 MeV. (b) Initial electron beam size with flux distribution: histogram distribution approximating truncated Gaussian distribution.

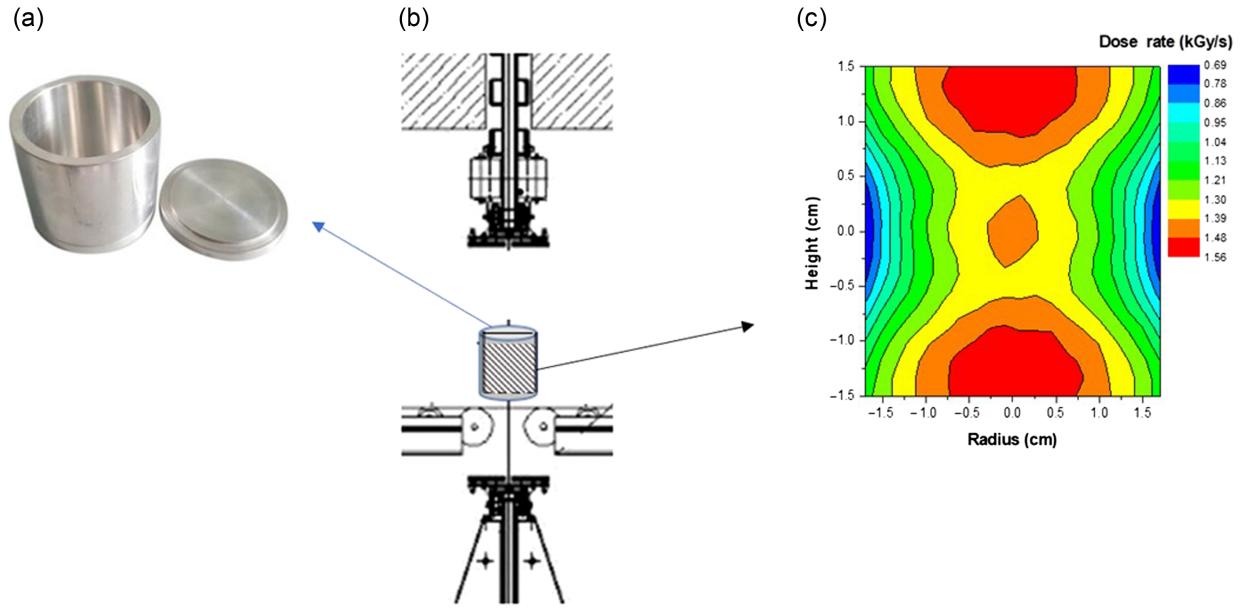

FIG. 7. Simulation of ETS-10 irradiation: (a) Al alloy holder; (b) 02 identical scanners; (c) dose map in the longitudinal section inside the zeolite sample.

beam size experiment. These tallies were positioned at 20, 30, 45, and 60 cm from the electron source to gather electron energy spectra. We then converted these energy values into dose rate values (in kGy s^{-1}) based on the intensity and operating power of the UERL-10-15S2 linac system at our facility: divided the total recorded energy in tally F8 by the mass of the tally's cell and then multiplied the result by the flux of electrons emitted from the source.

C. Simulation of zeolite ets-10 irradiation

To investigate the dose distribution in the electron-irradiated sample, we used the e-beam profile configuration mentioned above to simulate the irradiation of zeolite ETS-10. The simulation built a 2D dose map and calculated the mean absolute percentage deviation (MAPD) of the absorbed dose rate [28] in the irradiated zeolite sample. We extended the configuration to two symmetrical scanners in this simulation section. The zeolite sample is placed in the middle position, about 36 cm apart from the two scan horns: stationary, double-sided mode.

ETS-10 zeolite is a titanosilicate with a chemical composition [35] of $[Si_{78}Ti_{16}O_{208}]Na_{23}K_9$ and average density of 1.75 g cm^{-3} [36]. Inheriting previous research results on the ability to degrade electron energy of Al alloy [28], the holder has been designed and machined as follows: the cylindrical box is machined from 1050 aluminum alloy, with an outer diameter of 4 cm, inner diameter of 3.4 cm, and height of 3 cm [Fig. 7(a)]; contains approximately 47.7 g of ETS-10; the Al alloy lid thicknesses are 0.25, 0.47, and 0.68 cm. The lid thicknesses were selected as above for the intention of irradiating ETS-10 with different energy distributions, with the most probable energy at 9, 8, and 7 MeV (Table III). Due to the symmetry of the two scan horns and the geometric symmetry (cylindrical) of the holder [Fig. 7(b)], the 2D dose map was investigated for the longitudinal section passing through the holder's symmetry axis [Fig. 7(c)].

III. RESULTS AND DISCUSSIONS

A. Mathematical description of the electron energy spectrum of the degraded e-beam passing a thin Al alloy plate

In the previous study [28], the electron energy distributions, obtained by tally F8, were fitted with our proposed mathematical function [Eq. (3)].

$$I(E) = I_o + Ae^{z+1-e^z},\ z = 2\frac{E-E_p}{w}, \tag{3}$$

where E, E_p, A, w, and I_o are the electron energy, most probable energy, peak height, full width at half maximum (FWHM), and distribution's offset, respectively. This function is an ansatz that helps describe the electron energy spectrum and conveniently determine the E_p and E_a values. Incidentally, this function has a form similar to the approximated Landau distribution [37,38]. The Landau distribution primarily describes the energy loss of electrons passing through a thin layer of matter [39]. In the case of the electron energy distributions remaining after electrons pass through thin aluminum plates in this study, these distributions could be neither described by the Landau distribution nor by the approximated Landau distribution. Instead, we modified the approximated Landau distribution by the method that the remaining energy would be the

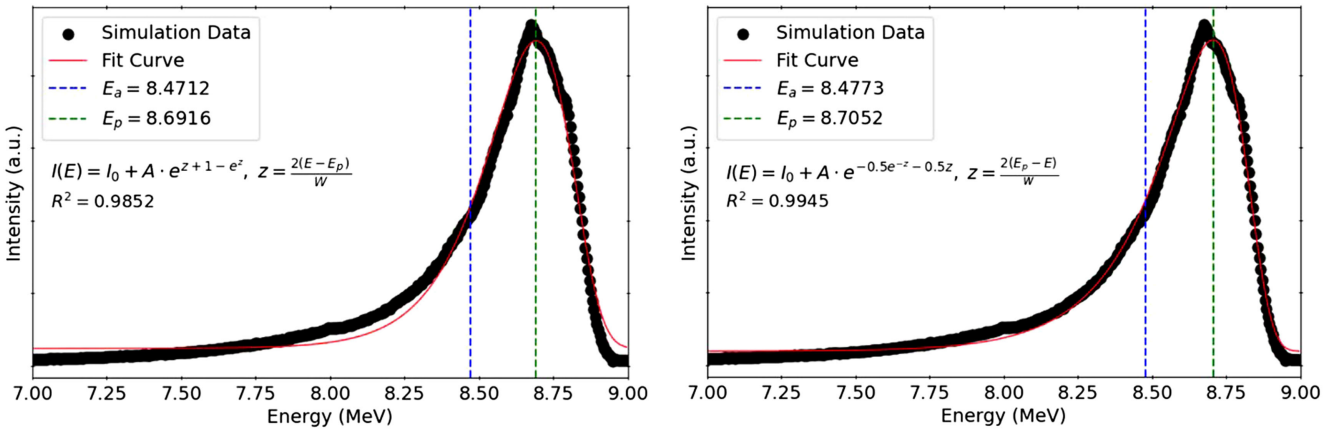

FIG. 8. Energy distribution of electron beam degraded by 0.3 cm Al alloy plate—comparison of two fit curves.

initial energy of the electron ($E_o \sim 10$ MeV) minus the energy lost (E_{loss}) due to ionization. Specifically, the distribution of remaining energy has the form $I(E_{\text{remain}}) = I(E_o - E_{\text{loss}})$. This method reflected and shifted the approximated Landau distribution to the energy region near E_o. By this approach, we got the modified mathematical function which fits better for the degraded electron energy distribution [Eq. (4)]. The fit is improved, and the new function is well applicable for the distributions of energy remaining of electrons passing through thin Al alloy plates in this research. Figure 8 illustrates the electron energy distribution passing through a 0.3 cm Al plate. This energy spectrum was fitted using both functions [Eqs. (3) and (4)]. The new fit curve is better with $R^2 = 0.995$ than the old one with $R^2 = 0.985$. The approach of modified approximated Landau distribution implies that the new function can accurately describe the physics of the distribution of energy remaining of fast charged particles passing through a thin layer of matter. However, to have a robust conclusion, a more thorough research must be conducted, such as different energies (a broader range of energy) and energy distributions of electron beams must be accounted for as well as different thicknesses of various materials.

$$I(E) = I_o + Ae^{-0.5z-0.5e^{-z}},\ z = 2\frac{-E+E_p}{w}. \quad (4)$$

We carried out the above nonlinear least-squares fitting using the Python programming language [40] version 3.12.4 with the curve_fit algorithm from the library SciPy 1.14.0. Additionally, libraries such as NumPy 1.26.0, PANDAS 2.2.2, and Matplotlib 3.9.1 were utilized to process data and present results graphically. To speed up the convergence of the algorithm, the initial parameters I_0, A, E_p, and w were set to 0.01, 0.015, 8.68, and 0.1. The average energy value E_a is calculated by the formula [Eq. (5)] [41]

$$E_a = \frac{\int_{E1}^{E2} EI(E)d(E)}{\int_{E1}^{E2} I(E)d(E)}. \quad (5)$$

E_1 and E_2 correspond to 7 and 9 MeV, respectively. We obtained R^2 value with the $r2$_score function from the library sklearn 0.0.post5.

B. Comparison of electron energy results between simulation and experiment

The E_p and E_a values from the simulation were determined by applying the new mathematical function [Eq. (4)] and curve_fit algorithm to the electron energy distributions recorded by tally F8. The results are presented in Table I, which are compared with the corresponding values obtained from the experimental procedure. The simulation uncertainty analysis was performed based on the initial energy error of 2.5%. The experimental error was calculated based on the propagation of the deviations of the trendline fit parameters. The energy correlation observed in both simulations and experiments is largely consistent.

TABLE I. Comparison of electron energy at 30 cm from scanner between simulation and experiment.

	Direct from the scanner		Degraded through 0.3 cm Al alloy plate		Degraded through 0.5 cm Al alloy plate		Degraded through 0.8 cm Al alloy plate	
Electron's energy (MeV)	E_p	E_a	E_p	E_a	E_p	E_a	E_p	E_a
Simulation	9.86 ± 0.25	9.82 ± 0.25	8.71 ± 0.22	8.48 ± 0.21	7.86 ± 0.20	7.24 ± 0.18	6.49 ± 0.16	5.57 ± 0.14
Experiment	9.76 ± 0.29	9.60 ± 0.38	8.42 ± 0.31	7.95 ± 0.40	7.52 ± 0.40	6.76 ± 0.50	6.16 ± 0.55	5.17 ± 0.68
Relative difference (%)	1.01	2.24	3.33	6.25	4.33	6.63	5.08	7.18

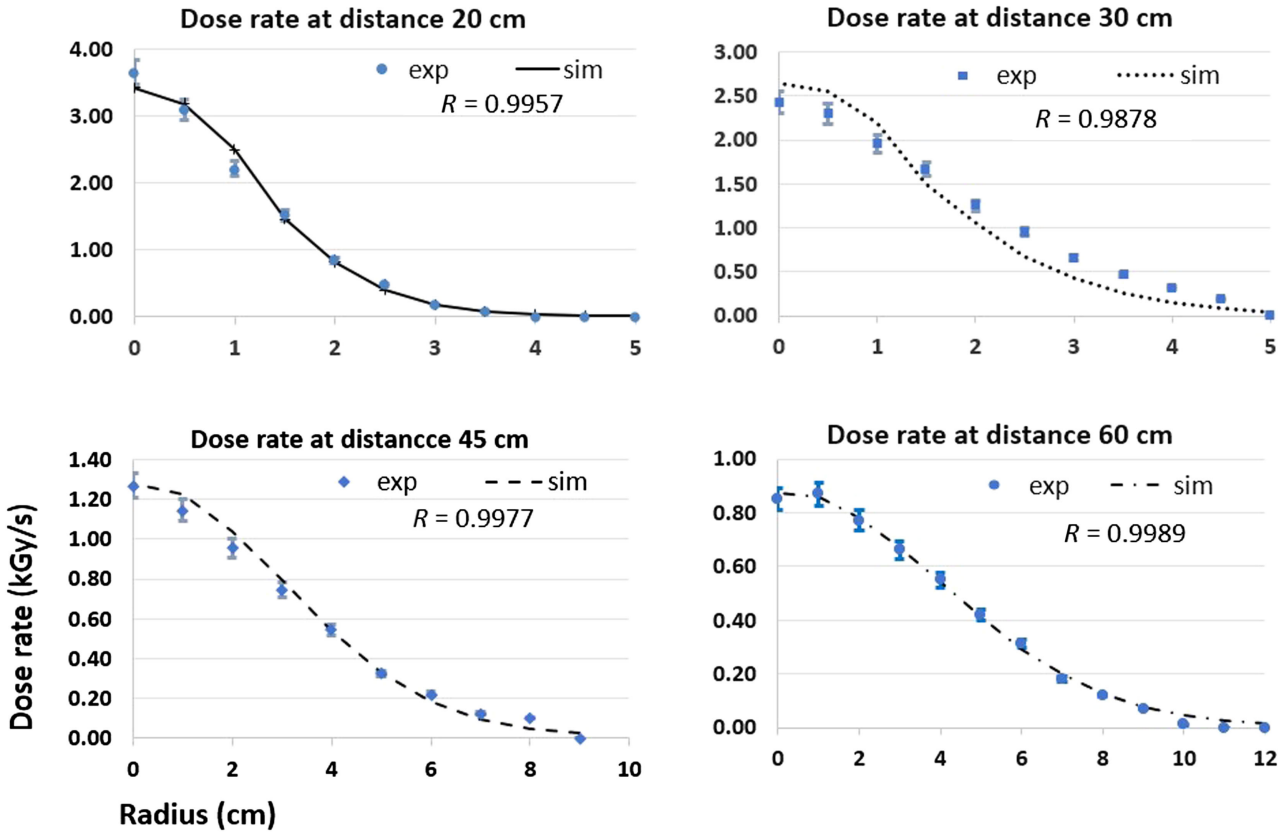

FIG. 9. Comparison of experiment and simulation dose rates at various distances to the scan horn.

However, the energy values obtained from the experiments tend to be lower than those from the simulations, particularly in the low-energy range. Notably, as the energy decreases, the discrepancy between the two methods increases. The cause is that the simulation using tally F8 directly captures the electron energy distribution, whereas, in our experiments, we do this indirectly by measuring the depth-dose curve and then extrapolating the electron energy. The initial e-beam energy error also affects the discrepancy. Another reason for the issue is that the electron energy distribution through the aluminum plates has degraded, resulting in a less concentrated distribution compared to the initial distribution that is emitted directly from the scanner. Due to the above reasons, the experimental deviation becomes more prominent when the electron energy is degraded and the energy distribution is more dispersed. Therefore, we recommend using the Riso Wedge energy measurement method for e-beam with a concentrated (sharp) energy distribution.

C. Comparison of beam size results between simulation and experiment

As described in Sec. II A 2, the beam size is determined using B3 dosimeters measuring dose in 8 to 10 s, then normalized to the dose value in one second, i.e., dose rate (kGy s^{-1}). The simulated and experimental results were compared after being normalized to the dose rate value. In Fig. 9, the experimentally measured and simulated dose rates are compared separately at each distance from the upper scanner. The dose rate distribution is according to the radius, which is the distance from the scan horn axis (longitudinal section). We estimated the correlation between simulation and experimental data using the Pearson correlation coefficient. The correlation coefficients are all above 0.985 (Fig. 9). These R coefficients indicate that the correlation between simulation and experiment is good. At distances close to the scanner of 20 and 30 cm, the simulation gives dose rates slightly different from the experiment. The possible causes of this difference are the uncertainty of the B3 dosimeter (about 4%–6% [30]), the uncertainty of the initial beam energy (which is stated in the linac description section), and the staggered-manner arrangement of the B3 dosimeters. However, at further distances of 45 and 60 cm, the distributions between the simulation and experiment match each other.

In Fig. 10, the dose rate distribution according to the radius (distance from the scan horn axis) corresponding to the distances to the scanner is fully reproduced on the same dose rate–radius graph. This graph gives us a visual representation of the beam size of the electron beam emitted by the scanner. Assuming these distributions are Gaussian, the beam spot's divergence angle can be calculated from the FWHM [Eq. (6)] of these distributions

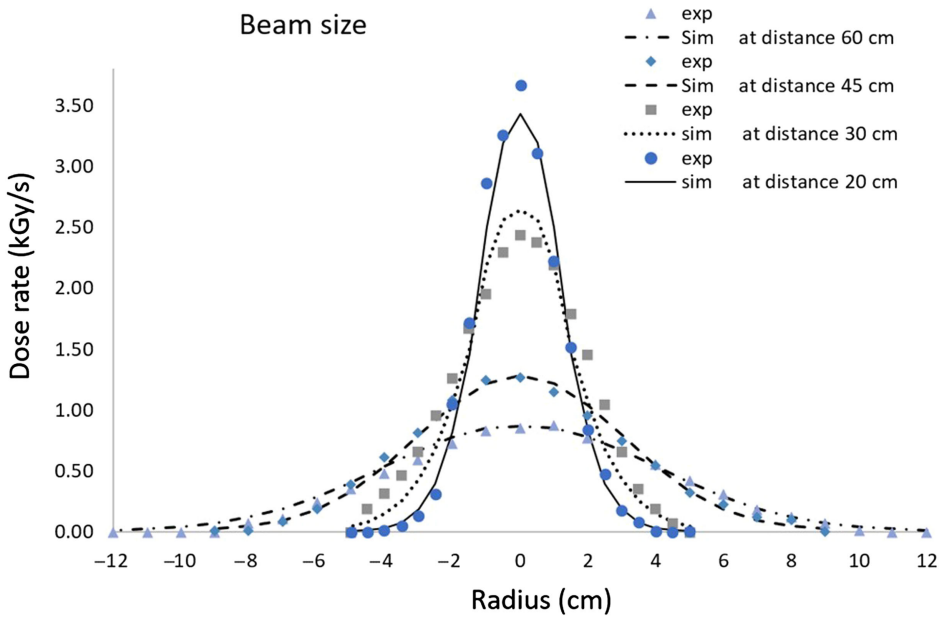

FIG. 10. Beam size between simulation and experiment.

(Table II); the average value of this angle is 4.12°. This represents the typical divergence angle of our facility's linac, which has a titanium window thickness of 61 μm.

$$\boldsymbol{\theta} = \boldsymbol{arctan}\left(\frac{\mathrm{FWHM_d} - \mathrm{FWHM_i}}{2{*}\boldsymbol{d}}\right), \tag{6}$$

where $\mathrm{FWHM_i} = 0.33$ cm is the initial full width half maximum of the initial beam spot, and d is the distance from the scan horn.

TABLE II. Beam spot's divergence angle.

Distance from the scanner d (cm)	$\mathrm{FWHM_d}$ (cm)	Beam spot's divergence angle (°)
60	9.79	4.51
45	7.34	4.45
30	4.46	3.94
20	2.82	3.56
Average		4.12

TABLE III. Results of ETS-10 irradiated simulation.

Al alloy lid thickness (cm)	0.68	0.47	0.25
Electron's most probable energy (MeV)	7.04	8.00	8.93
MAPD (%)	12.57	14.74	22.98
Minimum dose rate	0.69	1.10	1.01
Maximum dose rate	1.56	2.16	2.72
Average dose rate ($\mathrm{kGy\,s^{-1}}$)	1.28	1.54	1.79

D. Apply e-beam profile in ETS-10 irradiated simulation

This final simulation section utilizes a beam profile configuration that has been set up and confirmed with the experimental results shown above. The dose map within the zeolite sample is crucial for evaluating the properties of electron-irradiated ETS-10. In conjunction with MAPD, we can assess the relative uniformity of the dose. This information, along with the electron energy, helps us control the extent of the effects of electron irradiation on the sample and the uniformity of that impact.

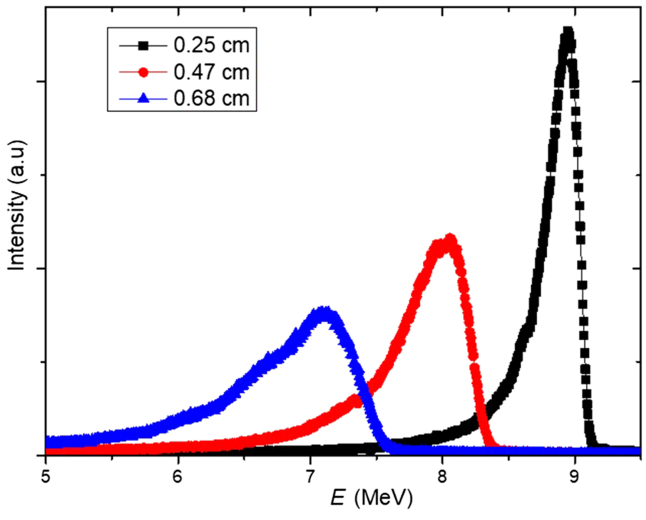

FIG. 11. Electron energy distributions irradiating the ETS-10 sample corresponding to various Al alloy lid thicknesses: 0.25, 0.47, and 0.68 cm.

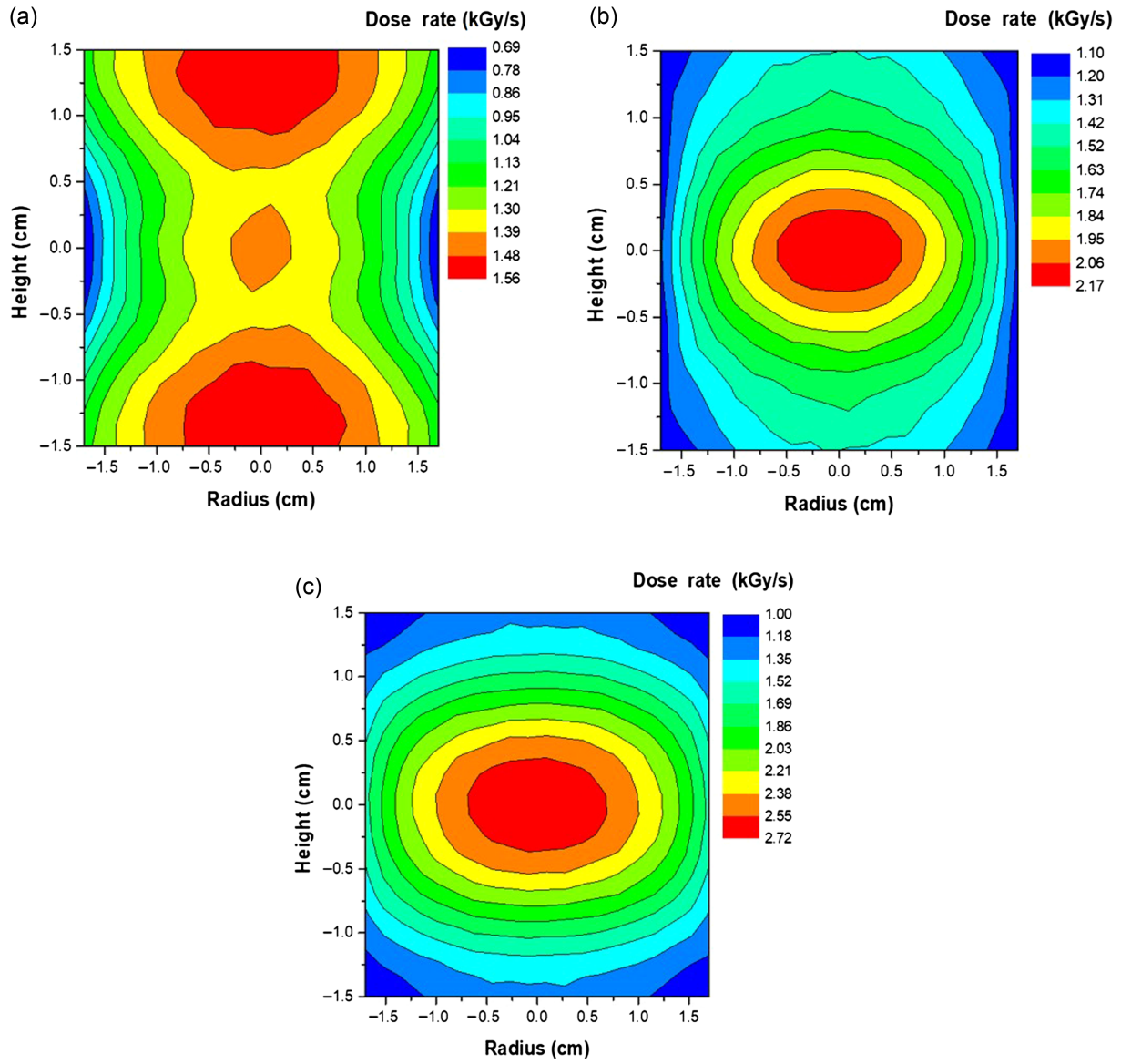

FIG. 12. Dose map in the irradiated ETS-10 zeolite contained inside an Al alloy holder with various lid thicknesses: (a) 0.68 cm, (b) 0.47 cm, and (c) 0.25 cm. Dose rate values are contour plotted using a linear color scale.

The results shown in Table III and Fig. 12 are intriguing; as the lid thickness increases, i.e., we irradiate the zeolite sample with energy distributions with decreasing peak energies of 9, 8, and 7 MeV (Fig. 11), MAPD (%) gradually decreases, meaning that the absorbed dose becomes more uniform in the sample. This observation is clearly illustrated by the longitudinal-sectional dose map of the ETS-10 sample inside the cylindrical holder. In Fig. 12(c), zeolite is irradiated by electrons with a concentrated energy distribution of 9 MeV, resulting in a highly concentrated absorbed dose in the central region of the sample. The MAPD in this case is relatively high, nearly 23%, showing that the impact of electrons on the material is not uniform, mainly in the central region of the sample. In Fig. 12(b), with decreasing irradiation energy, the dose distribution is still concentrated in the center of the holder but has also gradually expanded to the upper and lower boundary regions. In the energy distribution case with a peak of 7 MeV, the dose rate distribution has shifted its concentration toward the upper and lower boundaries, resulting in a more even spread throughout the sample [Fig. 12(a)]. Notably, we observe that the MAPD in this case has decreased to 12.57%. Although the dose rate is reduced compared to irradiation with higher energy electrons, in return we get uniform electron impact on the entire sample. The above dose map simulation results are due to the combined influence of many factors, such as the composition of ETS-10, the geometric structure of the Al alloy holder, and the e-beam profile, including electron energy distribution and beam size. The interaction between

electron and material is influenced primarily by the electron energy and electron stopping power of matter (depending on the density and the atomic number of the matter). According to the electron depth-dose profile, an example of electron interaction with Al alloy can be seen in Fig. 4, the absorbed dose will gradually increase to a maximum at a depth that depends on the electron stopping power of matter, and then will decrease quite rapidly to zero. In this study design, the ETS-10 is irradiated in double-sided mode, so the impact of electron radiation will be total from both sides. When high-energy electron transports into zeolite sample as in the 9 MeV case, the total electron impact will be maximum at the center of the zeolite sample [Fig. 12(c)]. In the case of electron energy distribution with a lower energy (7 MeV), the electron ranges will be shorter from both sides, leading to the electron impact being more evenly spread throughout the sample [Fig. 12(a)].

We can select the most optimal (and desired) irradiation configuration based on these simulated results to modify zeolite ETS-10. The irradiation dose level is more precisely controlled with information about the max-min range of absorbed dose and the corresponding irradiation time. The uniformity of irradiation dose is determined more accurately based on dose maps and MAPD parameters.

IV. CONCLUSION

In this paper, we investigated the electron beam profile in detail using both experiments and Monte Carlo simulations. The simulation configuration of the beam profile, specifically the initial electron beam, has been set up with two essential aspects: initial energy distribution and initial beam size with the flux distribution. The comparison results indicate that this beam profile confirms well with the experiment, which is an important improvement in electron irradiation research on the UERL-10-15S2 linac system. Another highlight feature of this study is that we proposed a new mathematical function by modifying the approximated Landau distribution. This new function provides a better fit than our previous mathematical function and, more importantly, accurately represents the physics of the energy spectrum of electrons passing through a thin layer of matter. Using this new function, we can calculate the average and most probable electron energies, E_a and E_p, more accurately, which is helpful in studying the e-beam energy distribution from accelerators. Furthermore, the function can contribute to setting up the energy remaining of the e-beam passing through a thin layer of matter in other electron irradiation studies, where the irradiated objects are often encapsulated in thin packaging or containers. Based on the results obtained from the experimental determination of electron energies with different electron energy distributions ranging from 6 to 10 MeV, we recommend using the Riso Wedge energy measurement method for e-beams with a sharp energy distribution.

Applying the above improvements and new features, we have simulated the irradiation modification of zeolite ETS-10. This simulation result helps us to choose the optimal irradiation configuration to modify zeolite. The irradiation dose levels will also be performed more accurately with the corresponding irradiation time. The dose uniformity is also determined more accurately through the dose map and MAPD parameters. The optimal irradiation configuration includes aspects such as irradiation electron energy, desired irradiation dose level, the max-min range of the dose rate, and the uniformity of absorbed dose in the material. With this information, the results of changes in the structure of ETS-10 under the effect of electron irradiation will be interpreted more accurately. Moreover, with the above beam profile configuration, we can simulate the design of irradiation studies on other research objects. The results from this study provide solutions to enhance the application of industrial linac systems in scientific research fields, especially research on irradiation modification of materials.

However, this study designed experiments and simulations on irradiated objects with small dimensions (compared to the scanning width of the scanner), such as the strip of B3 dosimeter and the cylindrical aluminum alloy holder. Therefore, the horizontal scanning effect of the beam is neglected. Further studies on irradiated sample objects with large horizontal dimensions need to consider the scanning effect of the e-beam and modify the initial beam configuration.

ACKNOWLEDGMENTS

This research was funded by the Vietnam National Foundation for Science and Technology Development (NAFOSTED) under Grant No. 103.02-2021.88. The authors also thank Nguyen Tat Thanh University, Ho Chi Minh City, Vietnam, for providing the facilities required to carry out this work.

A.-T. V.: programming and supporting algorithms; C. V. C.: investigation—performing the experiments and methodology; L. L. N.: computational and visualization; L. T. S.: computing resources and validation; P. T. P.: conceptualization, methodology, writing—original draft and supervision; V.-H. P.: writing—review and editing; and V.-P. D.: project administration and funding acquisition.

The authors declare that they have no known competing financial interests or personal relationships that could have appeared to influence the work reported in this paper.

DATA AVAILABILITY

All raw data corresponding to the findings in this manuscript are available within the article. Data support to the figures are not publicly available. The data are available from the authors upon reasonable request.

APPENDIX: LINEAR ACCELERATOR UERL-10-15S2 PARAMETERS

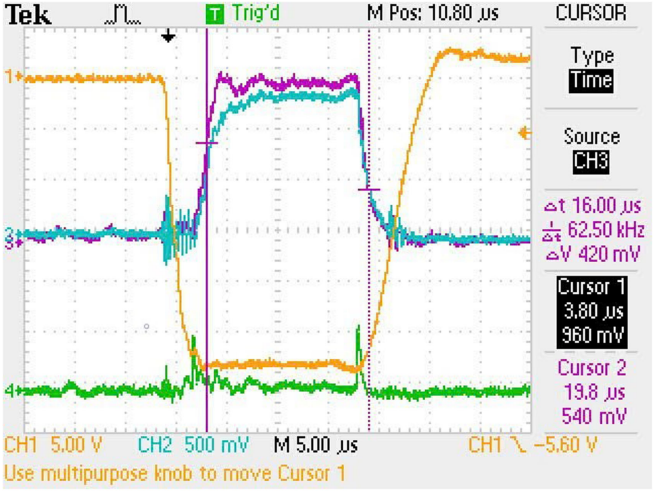

FIG. 13. Linear accelerator UERL-10-15S2: The oscilloscope traces of electron beam pulses (in purple and cyan), Klystron high voltage (in yellow), and reflected rf (in green).

[1] K. M. Morehouse and V. Komolprasert, Irradiation of food and packaging: An overview, ACS Symp. Ser. **875**, 1 (2004).

[2] A. Berejka, M. Cleland, and M. Walo, The evolution of and challenges for industrial radiation processing—2012, Radiat. Phys. Chem. **94**, 141 (2013).

[3] IAEA, Recent achievements on irradiation facilities, in *Proceedings of the Consultancy Meeting Report* (IAEA, Vienna, 2019), https://nucleus.iaea.org/sites/diif/resources/PublishingImages/Pages/default/Recent%20Achievements%20on%20Irradiation%20Facilities.pdf.

[4] V. C. Cao *et al.*, Treatment of dose nonuniformity inside star apples irradiated by 10 MeV electron beam, J. Radioanal. Nucl. Chem. **327**, 949 (2020).

[5] V. C. Cao, A.-T. Vo, Q.-T. Le, N.-T. Le, T. H. Duong, and H.-N. Tran, Depth-dose profiles in continuous and discontinuous materials of food products and medical devices irradiated by 10 MeV electron beam, J. Radioanal. Nucl. Chem. **330**, 609 (2021).

[6] I. V. Puhova, K. V. Rubtsov, I. Kurzina, A. V. Kazakov, and A. V. Medovnik, Modification of polymer materials by electron beam treatment, Key Eng. Mater. **670**, 118 (2016).

[7] L. A. Bursill, J. M. Thomas, and K. J. Rao, Stability of zeolites under electron irradiation and imaging of heavy cations in silicates, Nature (London) **289**, 157 (1981).

[8] Y. Yokota, H. Hashimoto, and T. Yamaguchi, Electron beam irradiation of natural zeolites at low and room temperatures, Ultramicroscopy **54**, 207 (1994).

[9] D. R. Acosta, G. Vázquez-Polo, R. Garcia, and V. M. Castaño, Electron beam degradation of Ca-A zeolite, Radiat. Eff. Defects Solids **127**, 37 (1993).

[10] J. Chen *et al.*, Electron beam irradiation-induced formation of defect-rich zeolites under ambient condition within minutes, Angew. Chem., Int. Ed. **60**, 14858 (2021).

[11] M. J. Jung, M. S. Park, and Y. S. Lee, Effects of e-beam irradiation on the chemical, physical, and electrochemical properties of activated carbons for electric double-layer capacitors, J. Nanomater. **1**, 2015 (2015).

[12] S. H. Kim, Y. J. Noh, S. N. Kwon *et al.*, Efficient modification of transparent graphene electrodes by electron beam irradiation for organic solar cells, J. Ind. Eng. Chem. **26**, 210 (2015).

[13] A. S. Pribytkov, O. P. Tkachenko, A. Yu. Stakheev, K. V. Klementiev, W. Grunert, M. W. E. van den Berg, L. M. Kustov, V. N. Golubeva, and A. V. Tel'nov, Effect of electron beam-irradiation on the structure and catalytic performance of Pd nanoparticles supported on Al_2O_3 and carbon, Mendeleev Commun. **16**, 254 (2006).

[14] D. Teweldebrhan and A. A. Balandin, Modification of graphene properties due to electron-beam irradiation, Appl. Phys. Lett. **94**, 013101 (2009).

[15] S. Gupta and R. J. Patel, Changes in the vibrational modes of carbon nanotubes induced by electron-beam irradiation: Resonance Raman spectroscopy, J. Raman Spectrosc. **38**, 188 (2007).

[16] A. Mayoral *et al.*, Direct atomic level imaging of zeolites: Oxygen, Na in Na-LTA and Fe in Fe-MFI, Angew. Chem., Int. Ed. Engl. **59**, 19510 (2020).

[17] S. Lotfy, A. Atta, and E. Abdeltwab, Comparative study of gamma and ion beam irradiation of polymeric nanocomposite on electrical conductivity, J. Appl. Polym. Sci. **135**, 46146 (2018).

[18] Y. Li, L. Li, and J. Yu, Applications of zeolites in sustainable chemistry, Chem **3**, 928 (2017).

[19] C. C. H. Lin, K. A. Dambrowitz, and S. Kuznicki, Evolving applications of zeolite molecular sieves, Can. J. Chem. Eng. **90**, 207 (2012).

[20] L. Xin, H. Sun, R. Xu, and W. Yan, Origin of the structure-directing effect resulting in identical topological open-framework materials, Sci. Rep. **5**, 14940 (2015).

[21] J. Cejka, Zeolites and ordered mesoporous materials: Progress and prospects, in *Proceedings of the 1st FEZA School on Zeolites, Prague*, edited by J. Cejka and H. van Bekkum, Studies in Surface Science and Catalysis Vol. 157 (Elsevier, Amsterdam, 2005), p. 11.

[22] Q. Sun, X. Hu, S. Zheng, Z. Sun, S. Liu, and H. Li, Influence of calcination temperature on the structural, adsorption and photocatalytic properties of TiO_2 nanoparticles supported on natural zeolite, Powder Technol. **274**, 88 (2015).

[23] M. C. Silaghi, C. Chizallet, J. Sauer, and P. Raybaud, Dealumination mechanisms of zeolites and extra-framework aluminum confinement, J. Catal. **339**, 242 (2016).

[24] T. N. Phuong, P. N. X. Vo, L. P. Trinh-Le, D. T. Pham, P. D. Phan, C. V. Cao, T. V. Tran, T. N. Luong, Q. L. M. Ha, and N. Le-Phuc, Role of e-beam irradiation treatment on detemplation and structural hierarchy of ZSM-5 zeolite, Microporous Mesoporous Mater. **315**, 110928 (2021).

[25] ISO/ASTM 51649-2015, *Practice for Dosimetry in an Electron Beam Facility for Radiation Processing at Energies Between 300 keV and 25 MeV*, 3rd ed. (ASTM International, West Conshohocken, PA, 2015).
[26] R. B. Miller, *Electronic Irradiation of Foods: An Introduction to the Technology* (Springer, New York, 2005).
[27] L. L. Nguyen *et al.*, Electron-beam irradiation of ZSM-5 catalyst with a designed sample holder: Simulation and experiment, Nucl. Eng. Technol. **57**, 103287 (2025).
[28] P. T. Phuc *et al.*, Design of a unique holder for structural modification of ZSM-5 zeolite using a 10 MeV electron beam generated from an industrial UERL-10-15S2 linear accelerator, Radiat. Phys. Chem. **174**, 108948 (2020).
[29] Ebeam energy estimation using the Risø Wedge, GEX Doc No. 100-260, 2024, https://www.gexcorp.com/doclibrary.html [accessed October 2024].
[30] B3 radiochromic film dosimeters, https://www.gexcorp.com/b3-dosimeters.html (2024) [accessed October 2024].
[31] Measuring GEX B3 dosimeters, GEX Doc No. 100-258, 2024, https://library.gexcorp.com/?wpdmdl=689 [accessed October 2024].
[32] B3 film strips or sheets, technical and usage information, https://library.gexcorp.com/?wpdmdl=585 (2024) [accessed October 2024].
[33] J. A. Kulesza *et al.*, MCNP® code version 6.3.0 theory & user manual, Technical Report No. LA-UR-22-30006, Rev. 1, Los Alamos National Laboratory, Los Alamos, NM, 2022.
[34] S. V. Kutsaev, Electron bunchers for industrial RF linear accelerators: Theory and design guide, Eur. Phys. J. Plus **136**, 446 (2021).
[35] A. Philippou, J. Rocha, and M. W. Anderson, The strong basicity of the microporous titanosilicate ETS-10, Catal. Lett. **57**, 151 (1999).
[36] V. Martin-Gil, A. López, P. Hrabanek, R. Mallada, I. F. J. Vankelecom, and V. Fila, Study of different titanosilicate (TS-1 and ETS-10) as fillers for mixed matrix membranes for CO_2/CH_4 gas separation applications, J. Membr. Sci. **523**, 24 (2017).
[37] S. Behrens and A. C. Melissinos, Landau distribution approximation for energy loss calculations, University of Rochester Report No. UR-776, University of Rochester, 1981.
[38] C. Grupen, Physics of particle detection, AIP Conf. Proc. **536**, 3 (2000).
[39] L. Landau, On the energy loss of fast particles by ionization, J. Phys. (USSR) **8**, 201 (1944).
[40] Python 3.12.4, https://www.python.org/downloads/release/python-3124/ (2024) [accessed October 2024].
[41] G. F. Knoll, *Radiation Detection and Measurement*, 3rd ed. (Wiley, New York, 1999).